


Anisotropic transport and multiple topology in quasi-one-dimensional ternary telluride NbNiTe₅Wen-He Jiao^{1,*}, Shaozhu Xiao^{2,†}, Wei Liu², Yi Liu¹, Hang-Qiang Qiu³, Keqi Xia⁴,
Shaolong He², Yuke Li⁴, Guang-Han Cao^{5,6} and Xiaofeng Xu^{1,‡}¹Key Laboratory of Quantum Precision Measurement of Zhejiang Province, Department of Applied Physics,
Zhejiang University of Technology, Hangzhou 310023, China²Ningbo Institute of Materials Technology and Engineering, Chinese Academy of Sciences, Ningbo 315201, China³Department of Applied Physics, Zhejiang University of Science and Technology, Hangzhou 310023, China⁴School of Physics and Hangzhou Key Laboratory of Quantum Matters, Hangzhou Normal University, Hangzhou 311121, China⁵School of Physics, Interdisciplinary Center for Quantum Information,
and State Key Lab of Silicon Materials, Zhejiang University, Hangzhou 310058, China⁶Collaborative Innovation Centre of Advanced Microstructures, Nanjing 210093, China (Received 18 January 2023; revised 20 April 2023; accepted 20 April 2023; published 12 May 2023)

Topological quantum materials, which feature nontrivial band topology, have been one of the most attractive research topics in condensed-matter physics in recent decades. The low-dimensional topologically nontrivial materials are especially appealing due to the rich implications for topological physics and the potential applications in next-generation spintronic devices. Here, we report the crystal growth, anisotropic magnetotransport, Hall effect, and quantum de Haas–van Alphen (dHvA) oscillations of a quasi-one-dimensional ternary telluride NbNiTe₅. The pronounced dHvA oscillations under $H \parallel b$ reveal three major oscillation frequencies $F_\alpha = 136.41$ T, $F_\beta = 240.34$ T, and $F_\gamma = 708.03$ T and the associated light effective masses of charge carriers. From the angular dependence of dHvA oscillations, we have revealed the identified frequencies exhibit anisotropic character, all of which arise from the holelike Fermi surface sheets formed by band 1 (F_α and F_β) and band 2 (F_γ) by comparing with the Fermi surface calculations. First-principles calculations demonstrate that NbNiTe₅ is a candidate of multiple topological material. In addition to the nonsymmorphic symmetry-protected nodal lines and band inversion (anticrossing) induced topological surface states, a ladder of topological gaps with the coexistence of strong and weak topology and a series of induced topological surface states are also identified.

DOI: [10.1103/PhysRevB.107.195124](https://doi.org/10.1103/PhysRevB.107.195124)**I. INTRODUCTION**

The field of new topological semimetals (TSMs), i.e., Dirac semimetals (DSMs), Weyl semimetals (WSMs), nodal-line semimetals (NLSMs), and nodal-surface semimetals (NSSMs), has been blossoming ever since the classification of materials based on symmetry and topology has been extended from insulators to metals or semimetals [1,2]. When the symmetry-protected crossing or touching of conduction and valence bands of semimetals can be characterized by a topological invariant [3], the semimetals are referred to as TSMs [4]. In DSMs and WSMs, two doubly or singly degenerate bands cross each other at discrete zero-dimensional (0D) nodal points and form a fourfold Dirac point or a twofold Weyl point [5–9]. In NLSMs, fourfold or twofold crossings extend along 1D lines, or closed loops, or even chains in momentum space [10,11], in contrast with discrete nodal points in conventional DSMs or WSMs. The Dirac or Weyl fermions in those topological materials could manifest themselves in many exotic quantum phenomena such as high carrier mobility [12],

unusual magnetic transport behaviors [13–15], and nontrivial quantum oscillations [16,17], etc., paving the way for vast material functionalities and applications in future devices and technologies.

A Dirac nodal-line state that is robust against spin-orbit coupling (SOC) usually occurs in 3D or at least 2D systems [11,18] and is rarely identified in quasi-1D materials, i.e., 2D systems with in-plane anisotropy [19], because additional crystalline symmetries (e.g., mirror or nonsymmorphic symmetry) are required to protect an extended linelike band crossing [20,21]. Recently, we discovered evidence of nontrivial topological metallic phases via a combination of an experimental study and first-principles calculations in low-dimensional ternary tellurides Ta TM Te₅ ($TM = \text{Pd, Ni, Pt}$) [22–24], the 2D atomic layer of which is composed of alternating quasi-1D $TM\text{Te}_2$ and TaTe₃ chains. Later, Hao *et al.* reported the realization of multiple Dirac nodal lines robust against SOC with fourfold degeneracy in TaNiTe₅ by angle-resolved photoemission spectroscopy (ARPES) as a result of the interplay between structural anisotropy and nonsymmorphic symmetry therein [19]. By means of ARPES measurements, we subsequently observed multiple Dirac-like nodal lines at the Brillouin zone boundary of TaPtTe₅ [25]. After theoretical analysis, we also concluded that the nodal lines along the Y - T path and connecting the R points are

*whjiao@zjut.edu.cn

†xiaoshaozhu@nimte.ac.cn

‡xuxiaofeng@zjut.edu.cn

robust against SOC and protected by nonsymmorphic symmetry. More interestingly, ferroelectric-like polarization together with novel surface states on the surface of TaNiTe₅ are observed by combining ARPES, scanning tunneling microscopy, and piezoresponse force microscopy measurements [26]. Very recently, the coexistence of strong and weak topological orders was unambiguously revealed in TaNiTe₅ through high-resolution ARPES and spin-resolved ARPES combined with theoretical calculations [27]. All of these breakthroughs demonstrate this class of low-dimensional materials to be an interesting platform to investigate the novel quantum states of matter and their coexistence, especially the relation between low-dimensional structure and topological physics.

In view of the rich physical properties among quasi-1D ternary tellurides TaTMTe₅ ($TM = \text{Pd, Ni, Pt}$), it is intriguing to explore the novel quantum states in the isostructural Nb-based homologue NbNiTe₅, which was first synthesized in 1987, and the physical properties of which are already known to be very limited, i.e., it is merely a good metal with Pauli paramagnetism [28]. In this work, we report the crystal growth of large-size NbNiTe₅ crystals via a self-flux method and their physical properties via comprehensive transport and magnetic measurements. The de Haas–van Alphen (dHvA) oscillations with the field applied along the normal-to-layer direction reveal three relatively light effective masses of the carriers. From the angle-dependent dHvA oscillations, we also reveal that the identified frequencies exhibit anisotropic characters. Our first-principles calculations not only suggest nontrivial band topology in NbNiTe₅, which is in a robust Dirac nodal-line phase like TaTMTe₅ ($TM = \text{Ni, Pt}$) [19,25], but they also show good consistency with the experimental data. Importantly, our results also identify a ladder of topological gaps with the coexistence of strong and weak topology and a series of induced topological surface states, in addition to the robust nodal lines protected by nonsymmorphic symmetry and topological surface states induced by band inversion (anticrossing).

II. EXPERIMENTAL METHODS

A. Sample synthesis

High-quality NbNiTe₅ single crystals were grown using a Te self-flux method [22–24,29]. The starting materials niobium (Nb, 99.95%) powder, nickel (Ni, 99.99%) powder, and tellurium (Te, 99.99%) powder were weighed in a molar ratio of Nb : Ni : Te = 1 : 1 : 9. The mixture was put into an alumina crucible, which was then loaded in a quartz ampoule. All the procedures mentioned above were carried out in a glove box filled with highly pure argon gas (O_2 and $\text{H}_2\text{O} < 0.1$ ppm). Subsequently, the quartz ampoule was removed from the argon glove box, evacuated with a rotary pump, and sealed under a vacuum condition. It was sequentially heated up to 1173 K and held for 6 h, slowly cooled down to 923 K over the course of 5 days, and finally centrifuged to separate the crystals from the excess Te. The air-stable single crystals with a shiny gray-black flattened needle-like shape were finally obtained. The size of the as-grown crystals is up to $4 \times 2 \times 0.3$ mm³, typical for this method, but very uncommon for crystals of quasi-1D tellurides [see the pho-

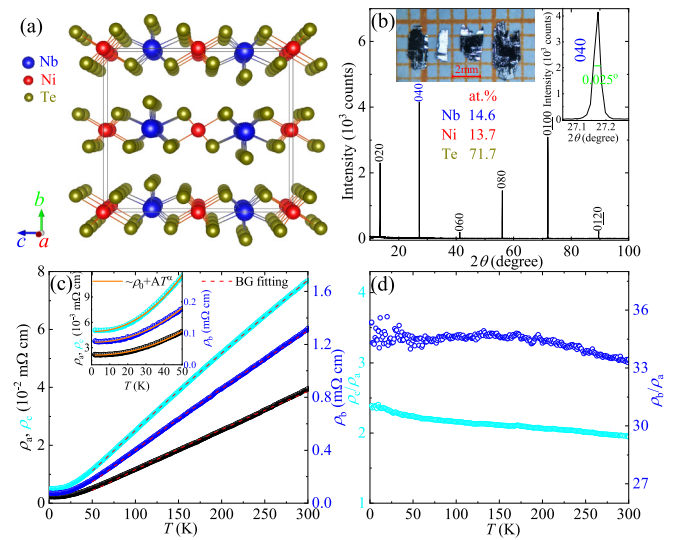


FIG. 1. (a) The crystallographic structure of NbNiTe₅ with an orthorhombic unit cell viewed perspectively along the a axis. (b) Single-crystal x-ray diffraction pattern at room temperature. The right inset enlarges the second reflection in the x-ray diffraction pattern. The left inset is a photograph of the as-grown NbNiTe₅ crystals on a millimeter paper. (c) Temperature dependence of the electrical resistivity ρ_a , ρ_c , and ρ_b with the current applied along three crystallographic directions. The dotted red lines correspond to the fits to the BG equation above 50 K. The insets enlarge the low- T dependence of ρ_a , ρ_c , and ρ_b below 50 K, all of which can be fitted using a power-law dependence T^α (the solid orange lines). (d) Temperature dependence of the resistivity anisotropy ρ_c/ρ_a (left axis) and ρ_b/ρ_a (right axis).

tographic image shown in the left inset of Fig. 1(b)], which enables the as-grown crystals suitable for various physical property measurements.

B. Structure and composition determination

X-ray diffraction (XRD) data acquisition was performed at room temperature with monochromatic Cu $K\alpha 1$ radiation using a PANalytical x-ray diffractometer (Model EMPYREAN) radiation by a conventional θ - 2θ scan for a crystal mounted on the sample holder. Energy-dispersive x-ray spectroscopy (EDS) was carried out using the Hitachi S-3400 instrument to get the chemical composition of the as-grown crystals. EDS analysis was performed on the fresh surface of the selected crystals, which gives the average composition of Nb_{1.02}Ni_{0.95}Te_{5.00}, very close to the stoichiometric NbNiTe₅. The detailed EDS results are tabulated in Table S1 of the supplemental material (SM) [30]. We plotted the crystal structure with the software VESTA [31].

C. Physical property measurements

The (magneto)transport measurements, including resistivity and Hall effect measurements, were performed in the Physical Property Measurement System (PPMS-9, Quantum Design) with the standard four-probe method. The Hall-effect measurement was performed by reversing the field direction. A small field-symmetric component due to mis-

aligned electrodes was subtracted from the Hall data. The Hall data are shown in Fig. S1 of the SM with the related discussion included. Magnetic susceptibility was measured on a 7 T magnetic property measurement system (MPMS-7, Quantum Design). The angular dependence of dHvA oscillations was measured using a homemade sample holder.

D. Band-structure calculations

The theoretical electronic structures of NbNiTe₅ were obtained by employing relativistic first-principles calculations based on density-functional theory (DFT) as implemented in the QUANTUM ESPRESSO code [32]. The exchange correlation potential energy was approximated by the generalized gradient approximation (GGA) using the PBE functionals [33]. The plane-wave kinetic cutoff energy was set to be 80 Ry. The Brillouin zone was sampled with a \mathbf{k} mesh of $14 \times 4 \times 8$ for self-consistent calculations, and $51 \times 21 \times 31$ for the calculations of three-dimensional Fermi surfaces. The extremal-orbit quantum oscillation frequencies were extracted from the calculated Fermi surfaces using the Supercell K-space Extremal Area Finder (SKEAF) code [34]. To obtain the surface-state spectrum, a first-principles tight-binding model Hamiltonian based on maximally localized Wannier functions was constructed by fitting the DFT band structures using WANNIER90 code [35]. The Nb $-d$ orbital, Ni $-d$ orbital, and Te $-p$ orbital were used for the initial projection. The surface-state spectra of NbNiTe₅ were calculated using the Green-function method as implemented in the WANNIERTOOLS package [36].

III. RESULTS AND DISCUSSION

As reported in Ref. [28], NbNiTe₅ crystallizes in the space group $Cmcm$ with the following lattice parameters: $a = 3.656 \text{ \AA}$, $b = 13.075 \text{ \AA}$, $c = 15.111 \text{ \AA}$, and $\alpha = \beta = \gamma = 90^\circ$ (at 123 K), isostructural with Ta TM Te₅ ($TM = \text{Pd, Ni, Pt}$). The eclipsed stacking of the 2D atomic layer along the b axis through van der Waals interactions constitutes the crystal structure of NbNiTe₅, as displayed in Fig. 1(a). The layered slab is composed of two alternating unique 1D chains, i.e., NbTe₃ and NiTe₂, that run parallel to the a axis. Thus, its crystal morphology (a needlelike shape with a cleavable flat surface perpendicular to the b axis) as shown in the left inset of Fig. 1(b) fully reflects its structural characteristics. The XRD pattern of the crystals with the layered facet lying on the sample holder at room temperature is shown in Fig. 1(b). A set of observed diffraction peaks can be well indexed with the (0210) peaks, which suggests the crystallographic b axis is perfectly perpendicular to the layered facet of the crystal. The interplanar spacing can be calculated to be 6.559 \AA , very close to half of the reported lattice parameter b ($b/2 = 6.538 \text{ \AA}$). The full width at half-maximum of the diffraction is extremely small, e.g., only 0.025° for the (040) peak, indicating the high quality of our crystals. Figure 1(c) shows the temperature (T) dependence of electrical resistivity along three crystallographic axes at zero magnetic field. All three of the resistivities ρ_a , ρ_c , and ρ_b almost follow a linear- T dependence from 300 to 50 K and cross over to a power-law dependence below 50 K. The inset of Fig. 1(c) displays the enlarged view below 50 K, with the

fitting curves to the formula $\rho(T) = \rho_0 + AT^\alpha$. The power α is fitted to be 2.13, 2.16, and 2.11 for ρ_a , ρ_c , and ρ_b . A nearly quadratic T dependence suggests the electron-electron scattering dominates in the low- T region. In the high- T region (e.g., $T \geq 50 \text{ K}$), the quasilinear T dependence is usually ascribed to dominant electron-phonon scattering, which can be further modeled with the Bloch-Grüneisen (BG) formula [37]:

$$\rho(T) = \rho_0 + A \left(\frac{T}{\Theta_D} \right)^5 \int_0^{\frac{\Theta_D}{T}} \frac{x^5}{(e^x - 1)(1 - e^{-x})} dx, \quad (1)$$

where ρ_0 , A , and Θ_D are the residual resistivity, electron-phonon interaction constant, and Debye temperature, respectively. As shown by the red dotted lines in Fig. 1(c), this equation fits the experimental data well from 50 to 300 K, indicating the dominance of electron-phonon interaction at this temperature range. The fitting yields $\rho_0 = 2.20 \pm 0.01 \mu\Omega \text{ cm}$, $A = 0.12 \pm 0.01 \text{ m}\Omega \text{ cm}$, $\Theta_D = 237 \pm 2 \text{ K}$ for ρ_a , $\rho_0 = 6.00 \pm 0.01 \mu\Omega \text{ cm}$, $A = 0.21 \pm 0.01 \text{ m}\Omega \text{ cm}$, $\Theta_D = 212 \pm 2 \text{ K}$ for ρ_c , and $\rho_0 = 0.082 \pm 0.001 \mu\Omega \text{ cm}$, $A = 3.85 \pm 0.02 \text{ m}\Omega \text{ cm}$, $\Theta_D = 229 \pm 2 \text{ K}$ for ρ_b . The similar T -dependent behavior of ρ_a , ρ_c , and ρ_b is also reflected by the almost unchanged anisotropic resistivity ρ_c/ρ_a and ρ_b/ρ_a with the temperature as shown in Fig. 1(d). Meanwhile, the quasi-1D transport behaviors are clearly manifested by $\rho_a : \rho_c : \rho_b = 1 : 2.4 : 35.3$ at 2 K, and $1 : 1.9 : 33.4$ at 300 K.

Figures 2(a)–2(c) display the T -dependent transverse magnetoresistance (MR) under different current and field-direction configurations below 50 K. Upon increasing the field from 0 to 9 T, the T -dependent MR of ρ_a and ρ_b behaves similarly, while that of ρ_c is obviously different. When the applied field is ramped to 5 T and above, we can observe that the MR of ρ_c abnormally increases with decreasing temperature, resulting in a MR minimum at a “turn on” temperature T^* , and finally saturates to a plateau at low temperatures. The inset of Fig. 2(b) shows the evolution of T^* versus $\mu_0 H$, indicating T^* increases linearly with increasing the magnetic field at a rate of 3.9 K/T. Such a temperature behavior with a comparable rate is also observed in its Ta-based homologs Ta TM Te₅ ($TM = \text{Pd, Ni, Pt}$) [22–24] and some other topological semimetals such as WTe₂ [38] and TaSb₂ [39]. The magnetic-field-driven resistivity upturn followed by a resistivity plateau has been taken as a transport signature of conducting surface states, due to the Landau level quantization of relativistic Dirac electrons [40,41]. Besides, this behavior may not be indicative of a metal-insulator transition, but it may appear in trivial materials with a small residual resistivity, high mobilities, and low charge-carrier density obeying Kohler’s rule in a magnetic field [42]. Following the conventional definition, we present the field-dependent MR as $[\rho(\mu_0 H) - \rho(0 \text{ T})]/\rho(0 \text{ T})$ in Figs. 2(d)–2(f). As seen, $\Delta\rho_c/\rho_c(0 \text{ T})$ is the most pronounced and reaches 208.0% at 9 T and 2 K, which is nearly five times that of $\Delta\rho_b/\rho_b(0 \text{ T})$ (42.9%) and over nine times that of $\Delta\rho_a/\rho_a(0 \text{ T})$ (22.5%). The anisotropic transport properties indicate its anisotropic Fermi surfaces and the associated classical transport lifetime, reflecting the anisotropic electronic properties in this quasi-1D NbNiTe₅. In addition, the interchain $\Delta\rho_c/\rho_c(0 \text{ T})$ and $\Delta\rho_b/\rho_b(0 \text{ T})$ show a similar field dependence, and both of

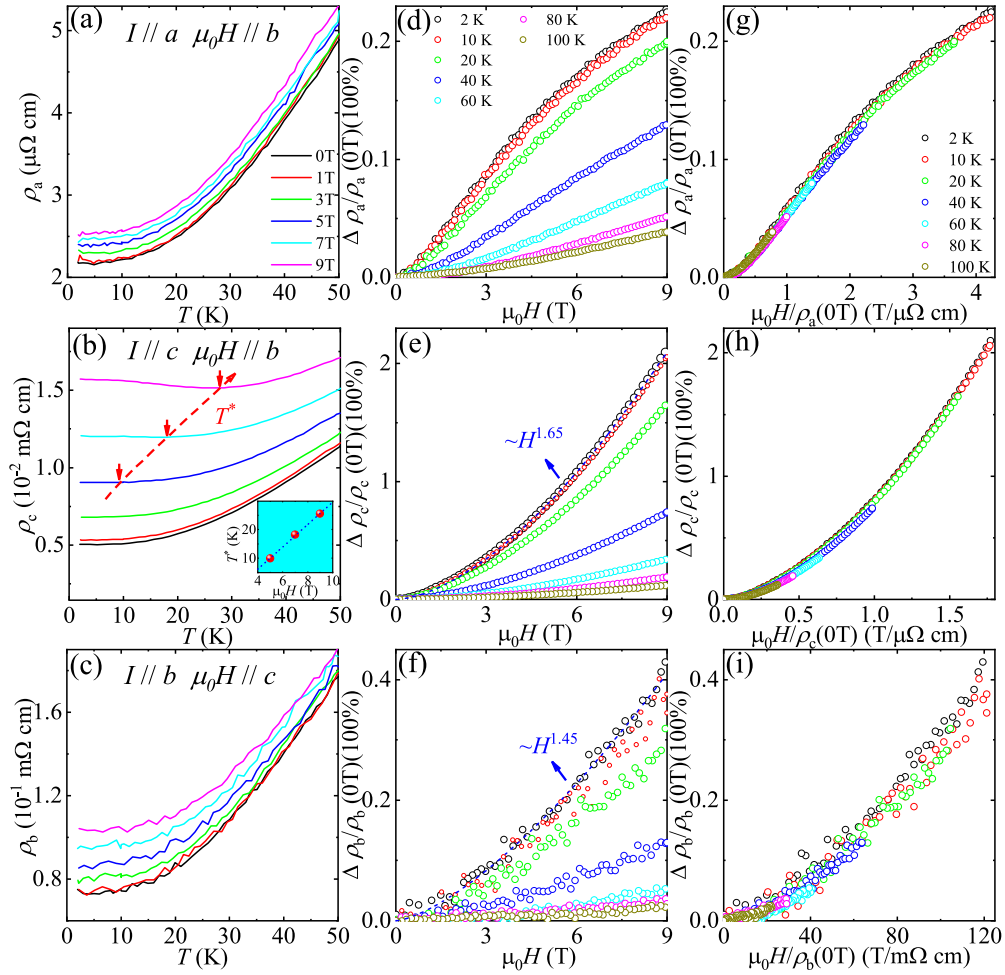


FIG. 2. Temperature dependence of ρ_a (a), ρ_c (b), and ρ_b (c) with the magnetic fields parallel to the b -axis, b -axis, and c -axis, respectively, up to 9 T below 50 K. The red arrows in (b) denote the temperature T^* . The inset shows the field-dependent T^* . The MR for ρ_a (d), ρ_c (e), and ρ_b (f) at several selected temperatures below 100 K. The blue dashed lines are the fits (see main text). Kohler's scaling for ρ_a (g), ρ_c (h), and ρ_b (i) at the corresponding temperatures.

them at 2 K can be well fitted to a single power law $\propto H^\alpha$ with $\alpha = 1.65$ and 1.45, while the field evolution of inter-chain $\Delta\rho_a/\rho_a(0\text{ T})$ shows a striking contrast, i.e., a seemingly quadratic field dependence in low field, but it crosses over to a quite linear dependence in higher field, especially at low temperatures. This behavior is also observed in its sister compound TaPdTe₅ [22], the origin of which remains controversial and deserves further investigations. Figures 2(g)–2(i) show Kohler's plots for the three configurations, from which we can find Kohler's rule is basically obeyed over a large temperature range for all.

In Fig. 3(a), we present the isothermal out-of-layer $\mathbf{H} \parallel b$ magnetization of a NbNiTe₅ single crystal measured up to 7 T at 1.8 K (the data at several other temperatures below 14 K are not shown here for clarity), which exhibits pronounced dHvA oscillations superimposed on a diamagnetic background. After removing a third-order polynomial background, the oscillations, which extend to a field ~ 2 T at 1.8 K and can sustain up to 14 K, become much more visible as displayed in Fig. 3(b). The fast Fourier transform (FFT) analysis of the oscillatory components reveals three oscillation frequencies $F_\alpha = 136.41$ T, $F_\beta = 240.34$ T, and

$F_\gamma = 708.03$ T, as shown in Fig. 3(c). The obtained frequencies indicate the existence of three extreme cross-sectional Fermi areas perpendicular to the b axis. Using the Onsager relation $F = \frac{Sh}{4e\pi^2}$ [43], where S is the extreme cross-sectional Fermi area perpendicular to the applied magnetic field and h is the Planck constant, we can calculate $S_\alpha = 12.99 \times 10^{-3} \text{ \AA}^{-2}$, $S_\beta = 22.89 \times 10^{-3} \text{ \AA}^{-2}$, and $S_\gamma = 67.43 \times 10^{-3} \text{ \AA}^{-2}$ for the three frequencies. By assuming a circular cross section, we can further estimate the Fermi wave vector k_F by the relation $k_F = \sqrt{\frac{S}{\pi}}$ using the obtained S . The corresponding S and k_F for three different pockets are listed in Table I, where the related parameters of its sister compound TaNiTe₅ are also included as a comparison.

In general, the oscillatory magnetization can be described using the 3D Lifshitz-Kosevich (LK) formula [43], which takes the Berry phase into account for a Dirac system [44]:

$$\Delta M \propto -R_T R_D R_S \sin \left[2\pi \left(\frac{F}{B} - \frac{1}{2} + \frac{\varphi_B}{2\pi} - \delta \right) \right], \quad (2)$$

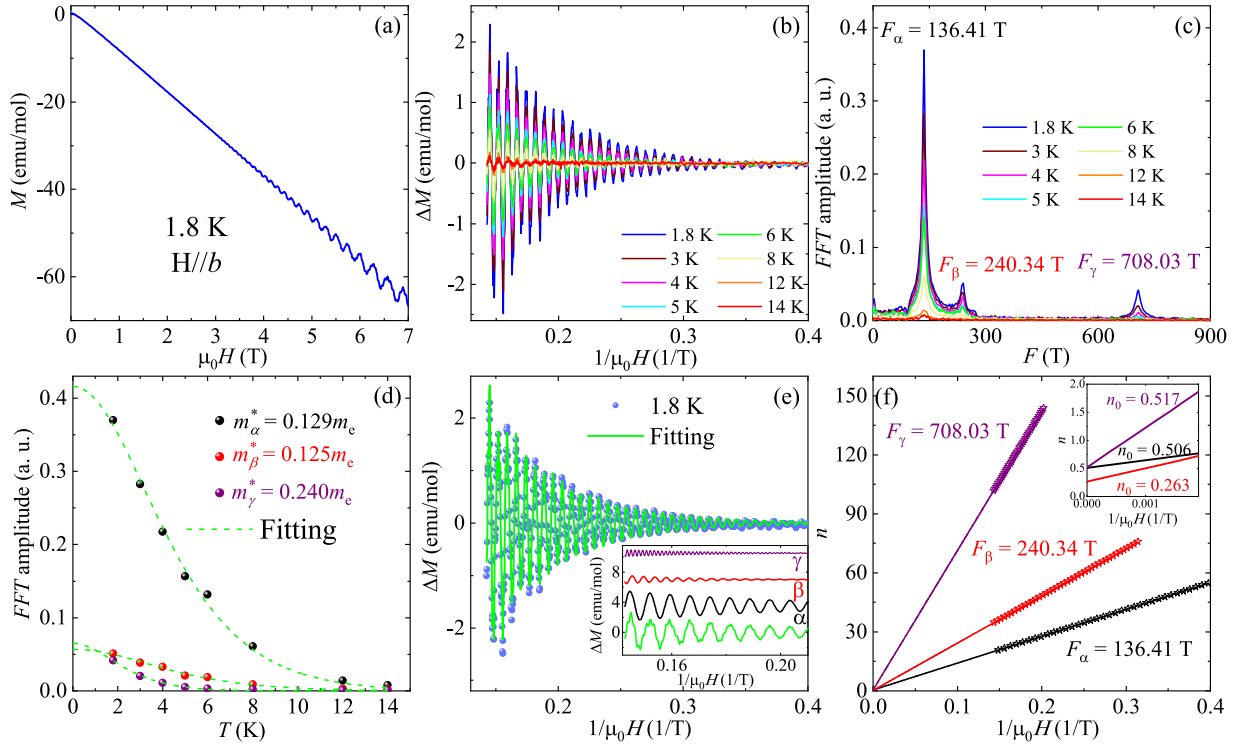


FIG. 3. The dHvA oscillations and nontrivial Berry phase of NbNiTe₅. (a) Isothermal magnetization under the $\mathbf{H} \parallel b$ -axis at 1.8 K. (b) The magnetization oscillations after subtracting the polynomial background at selected temperatures below 14 K. (c) The corresponding FFT spectrum. (d) The T -dependent FFT amplitude and the fit to R_T to determine the corresponding effective mass. (e) The Lifshitz-Kosevich fit (green line) of the oscillation pattern at 1.8 K. The inset shows the extracted three single-frequency oscillatory components, which are shifted vertically for clarity. (f) Landau's fan diagram for the identified frequencies F_α , F_β , and F_γ . The n -axis intercepts for each of the frequencies are illustrated in the inset.

where $R_T = \frac{2\pi^2 k_B m^* T / \hbar e \mu_0 H}{\sinh(2\pi^2 k_B m^* T / \hbar e \mu_0 H)}$, $R_D = \exp(2\pi^2 k_B T_D m^* / \hbar e \mu_0 H)$, and $R_S = \cos(\pi g m^* / 2m_e)$ are the thermal damping factor, Dingle damping term, and a spin-related damping term, respectively. m^* is the effective mass, T_D is the Dingle temperature, and φ_B is the Berry phase. The oscillation of ΔM is described by the sine term with the phase factor $-\frac{1}{2} + \frac{\varphi_B}{2\pi} - \delta$. The additional phase shift δ is determined by the dimensionality of the Fermi surface, and it is equal to 0 for a 2D Fermi surface and $\pm 1/8$ for a 3D Fermi surface. For the 3D case, the sign of δ depends on whether the probed S is minimal (+) or maximal (-) [45]. The T -dependent oscillation magnitude for all of the frequencies is shown in

Fig. 3(d), and it is fitted using R_T with the fitting parameter m^* for each orbit: $m_\alpha^* = 0.12(9)m_e$, $m_\beta^* = 0.12(5)m_e$, and $m_\gamma^* = 0.24(0)m_e$ (m_e is the bare electron mass). The small values of m^* imply the presence of relativistic charge carriers. With the fixed parameters of three effective masses and oscillation frequencies, the oscillation pattern at 1.8 K can be nicely fitted using the above LK formula, as shown in Fig. 3(e). The inset plots the extracted single-frequency oscillatory signals separately for clarity. The extracted Dingle temperature T_D and the quantum relaxation time τ_q obtained by the relation $\tau_q = \hbar / (2\pi k_B T_D)$, together with the corresponding m^* , are also listed in Table I. The quantum

TABLE I. Parameters extracted from dHvA oscillations of a NbNiTe₅ single crystal for three Fermi pockets. The parameters of TaNiTe₅ are also included as a comparison [23]. Here, F is the frequency in the FFT spectra, S is the extremal Fermi-surface cross-sectional area from the Onsager relation, k_F is the Fermi wave vector, m^* and m_e are the effective electron mass and the bare electron mass, respectively, T_D is the Dingle temperature, and τ_q is the quantum lifetime.

dHvA($B \parallel b$)	NbNiTe ₅			TaNiTe ₅			
	α	β	γ	1	2	3	4
F (T)	136.41	240.34	708.03	56	163	231	763
S (10^{-3} \AA^{-2})	12.99	22.89	67.43	53.30	15.52	22.00	72.67
k_F (10^{-2} \AA^{-1})	6.43	8.54	14.65	13.03	7.03	8.37	15.21
m^*/m_e	0.129	0.125	0.240	0.169	0.173	0.180	0.295
T_D (K)	8.48	23.16	8.12	5.26	5.97	7.17	6.34
τ_q (10^{-13} s)	1.43	0.53	1.50	2.31	2.04	1.70	1.92

mobility $\mu_q = e\tau/m^*$ for the three pockets is estimated to be $1947 \text{ cm}^2 \text{ V}^{-1} \text{ s}^{-1}$ (F_α), $745 \text{ cm}^2 \text{ V}^{-1} \text{ s}^{-1}$ (F_β), and $1098 \text{ cm}^2 \text{ V}^{-1} \text{ s}^{-1}$ (F_γ), respectively.

The derived φ_B are 1.02π , 0.75π , and 1.27π (F_α); 0.54π , 0.29π , and 0.79π (F_β); and 0.99π , 0.74π , and 1.24π (F_γ) for $\delta = 0$, $-1/8$, and $1/8$, respectively. Figure 3(f) presents the Landau level (LL) fan diagram for the three Fermi pockets [45], in an attempt to further evaluate the Berry phase. The minima of the dHvA oscillations are assigned as $n - 1/4$ (n denotes the integer LL indices). From the linear extrapolation in the fan diagram as shown in the inset of Fig. 3(f), three intercepts n_0 are 0.51 for F_α , 0.26 for F_β , and 0.52 for F_γ . From the values of these intercepts, the estimated Berry phase $\varphi_B = 2\pi(n_0 + \delta)$ is 1.02π for F_α , 0.52π for F_β , and 1.04π for F_γ . Moreover, the slopes of the LL fan diagram are 136.42, 240.37, and 707.87 T for the F_α , F_β , and F_γ bands, respectively. Therefore, all of these results are in excellent agreement with the results identified through the FFT analysis, demonstrating the validity of our analysis in NbNiTe₅. It is worth noting that a finite Berry phase, especially close to π , although usually used as evidence for topological nontrivial bands in the literature, may not be indicative of anything intrinsic to a 3D-Dirac Fermi surface but rather solely a consequence of time-reversal symmetry [46].

To clarify the morphology of the Fermi surface in NbNiTe₅, we performed angle-dependent quantum oscillation measurements with the magnetic field rotated from the b axis ($\mathbf{H} \parallel b$) to the c axis ($\mathbf{H} \parallel c$). After subtracting the polynomial background, the oscillation component, as shown in Fig. 4(a), displays a clear evolution of the angle θ , defined as the angle between the field direction and the b axis. The oscillation amplitude is suppressed gradually with increasing the tilted angle as a whole. Especially for $60^\circ \leq \theta \leq 80^\circ$, no trace of oscillatory component can be observed. The resultant FFT spectra for different angles are illustrated in Fig. 4(b). The oscillation frequencies F_α and F_β smoothly grow as the field is tilted towards $\mathbf{H} \parallel c$, and disappear for $\theta \geq 50^\circ$ and $\theta \geq 60^\circ$, respectively, whereas the high-frequency component F_γ is only distinguishable for $\mathbf{H} \parallel b$. There is one more frequency F_δ detected only at $\theta = 90^\circ$ in the FFT spectra. In Fig. 4(c), we summarize the angle dependence of each frequencies. To gain more quantitative information on the Fermi surface associated with the F_α and F_β bands, we have fitted θ -dependent data $F_\alpha(\theta)$ and $F_\beta(\theta)$ to the formula $F = F_{3D} + F_{2D}/\cos\theta$ for F_α and F_β , in which F_{2D} and F_{3D} denote the weight of 2D and 3D components. It is found that this formula can satisfactorily describe the data. For the F_α band, the relative weight F_{2D}/F_{3D} is ~ 7.3 , indicating the significant 2D character, while F_{2D}/F_{3D} is ~ 1.1 for the F_β band, suggesting the dimensionality between 2D and 3D.

To obtain a comprehensive understanding of the physical properties of NbNiTe₅, DFT calculations were employed to calculate the electronic structures of NbNiTe₅. In Figs. 5(a)–5(e), we show the 3D Fermi surfaces of the five bands that cross the Fermi level, from which we can explore the origins of the dHvA oscillations experimentally observed. When the external field is applied along the principal axis, it is easy to find some external orbits that contribute to the dHvA oscillations, e.g., the orbits H_1 , H_2 of band 1, H_3 of band 2, and E_1 of band 5 to a field along the b axis, and the orbits H_4 , H_5 of band

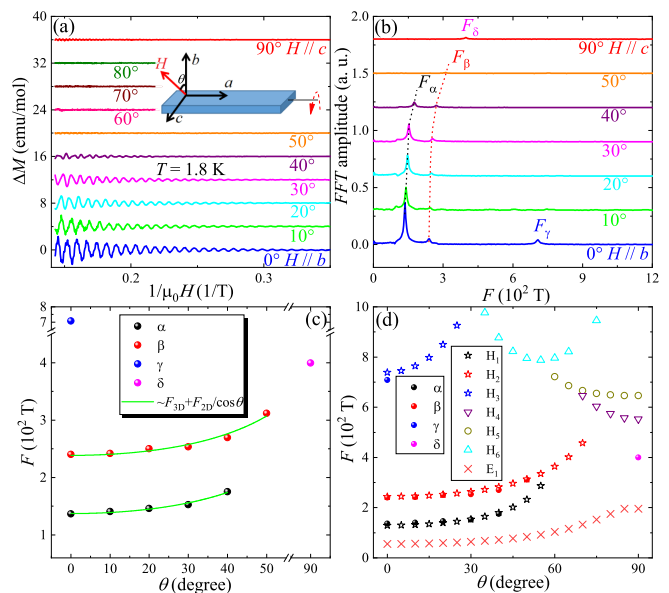


FIG. 4. Fermi surface morphology of NbNiTe₅. (a) The magnetization oscillations after subtracting the polynomial background at different angles ($T = 1.8 \text{ K}$). Data at different field orientations have been shifted for clarity. Angle $\theta = 0^\circ$ (90°) corresponds to $\mathbf{H} \parallel b$ -axis (c -axis). The measurement setup is plotted in the inset. (b) The corresponding FFT spectra at different angles. (c) The angular dependence of the oscillation frequencies. The green lines are fits to $F = F_{3D} + F_{2D}/\cos\theta$ for F_α and F_β . (d) The calculated and experimental angular dependence of dHvA frequencies. The open symbols are data based on the theoretical calculation, and the calculated data are plotted with the same color as the corresponding experimental data.

1 to a field along the c axis. As the external field gradually deviates from the principal axis, these orbits change accordingly before finally disappearing. To identify the origins of these oscillations, we calculate all possible θ -dependent extremal-orbit dHvA frequencies below $F < 1000 \text{ T}$ from the 3D Fermi surfaces, which are plotted in Fig. 4(d) with the experimental data included. It is straightforward to associate all three of the experimental frequencies F_α , F_β , and F_γ to the hole pockets H_1 , H_2 , and H_3 , respectively. The evolutions of F_α and F_β with θ show a perfect match with the calculations, whereas the frequency F_γ vanishes upon field rotation towards $\mathbf{H} \parallel c$, inconsistent with the calculation results. The theoretically predicted H_4 , H_5 , H_6 are also unobservable in our experimental data. The above-mentioned discrepancy can be due to distinctive characters (either a heavier effective mass or shorter scattering rate) of these bands resulting in a weaker, thus undistinguishable dHvA oscillation amplitude. Lower temperatures and higher magnetic fields might enable their observation. The frequency F_δ , only observable at $\theta = 90^\circ$, is not properly reproduced in the calculations.

Figures 5(g) and 5(h) show the calculated bulk bands without and with including SOC, respectively. Similar to TaPtTe₅, the bands on the plane Z-T-E-R-A ($k_3 = \pi$ plane) form Dirac nodal surfaces [25]. By comparing Figs. 5(g) and 5(h), it is obvious that the inclusion of SOC splits the bands on the plane Z-T-E-R-A except for path Z-T. That is, SOC breaks the nodal surfaces on the plane Z-T-E-R-A, but the topologically

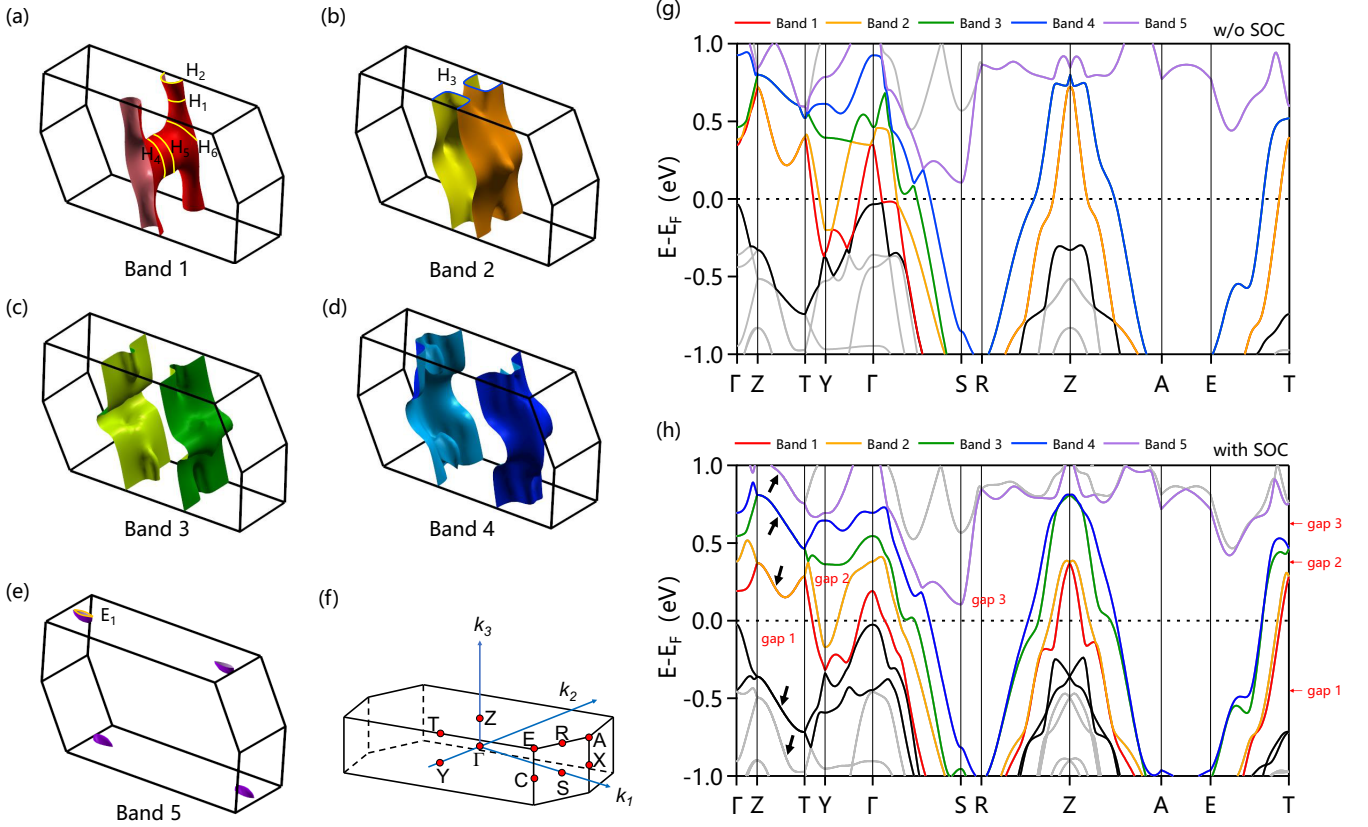


FIG. 5. (a)–(e) 3D Fermi surfaces of the bands 1–5 specified in (h) in the presence of SOC. The orbits H1–H6 and E1 in (a), (b), and (e) denote the pockets that contribute to the dHvA oscillations when the external field is applied along the direction from principal axes b to c . H represents the hole pocket, while E denotes the electron pocket. (f) Bulk Brillouin zone with high symmetric points labeled. (g),(h) Calculated band structures of NbNiTe₅ along high symmetric paths (g) without considering SOC and (h) with considering SOC. The black arrows in (h) indicate the topologically nontrivial Dirac nodal lines surviving against SOC.

nontrivial Dirac nodal lines on path Z-T survive against SOC, which are indicated by the black arrows in Fig. 5(h). The surviving nodal lines are protected by the nonsymmorphic symmetries in NbNiTe₅, which are also the common nature in TaTMTe₅ ($TM = \text{Ni, Pt}$) and originate from the cooperation between nonsymmorphic symmetry and structural anisotropy [19,25]. There are three continuous energy gaps (denoted with gap 1–3) across the Fermi level, as shown in Fig. 5(h). To identify the topological properties, we also calculated the bulk \mathbb{Z}_2 topological indices ($\nu_0; \nu_1\nu_2\nu_3$) of these gaps based on the Wilson loop calculations (see Figs. S2–S4 of the SM for details). The bulk \mathbb{Z}_2 topological numbers of these three gaps are (1;010), (0;010), and (0;010), respectively, indicating strong topology of gap 1 and weak topology of gaps 2 and 3. These gaps form a ladder of topological gaps with the coexistence of strong and weak topology, similar to that in monolayer PtBi₂ [47].

The bulk-boundary correspondence guarantees that the topological gap could induce a robust surface state on the sample surface. We choose three cleaved surfaces for studies: the top surface and two side surfaces A and B as denoted in Fig. 6(b). The top surface is easiest to obtain by cleaving between layers. The two side surfaces are perpendicular to the c axis and can be obtained by cleaving between Te-Te bonds. They are both Te-atom terminated but are different surfaces because of the different kinds of atoms underneath.

Figures 6(c), 6(e), and 6(g) show the calculated surface spectra of these three surfaces, respectively, which contain contributions of both bulk and surface states, and the corresponding spin-resolved surface spectra are illustrated in Figs. 6(d), 6(f), and 6(h), respectively. By comparing the spin-integrated surface spectra, spin-resolved surface spectra, and the surface spectrum of only the bulk states as shown in Figs. 6(i) and 6(j), a series of topological surface states can be identified, as labeled by SS1–SS6 in Figs. 6(c)–6(h). SS1 on the top surface and SS2, SS3 on the side surface are the different projections of the topological surface state originated from the strong topology of gap 1. SS2 sits entirely in the gap and is clearly distinguished, while SS1 and SS3 sit close to the boundary of the bulk state but still can be distinguished with the assistance of the spin-resolved spectrum. SS4–6 are not originated from the topology of the gaps 1–3, but are the different projections of the topological surface state originated from the band inversion (anticrossing) between band 1 and band 2 on path Y- Γ [Fig. 5(h)], which is similar to that reported in TaNiTe₅ [27]. The weak topology of energy gap 3 also yields topological surface states, which are shown in Fig. S5 of the SM.

IV. SUMMARY

In summary, we have carried out comprehensive studies on the physical properties of the quasi-1D ternary telluride

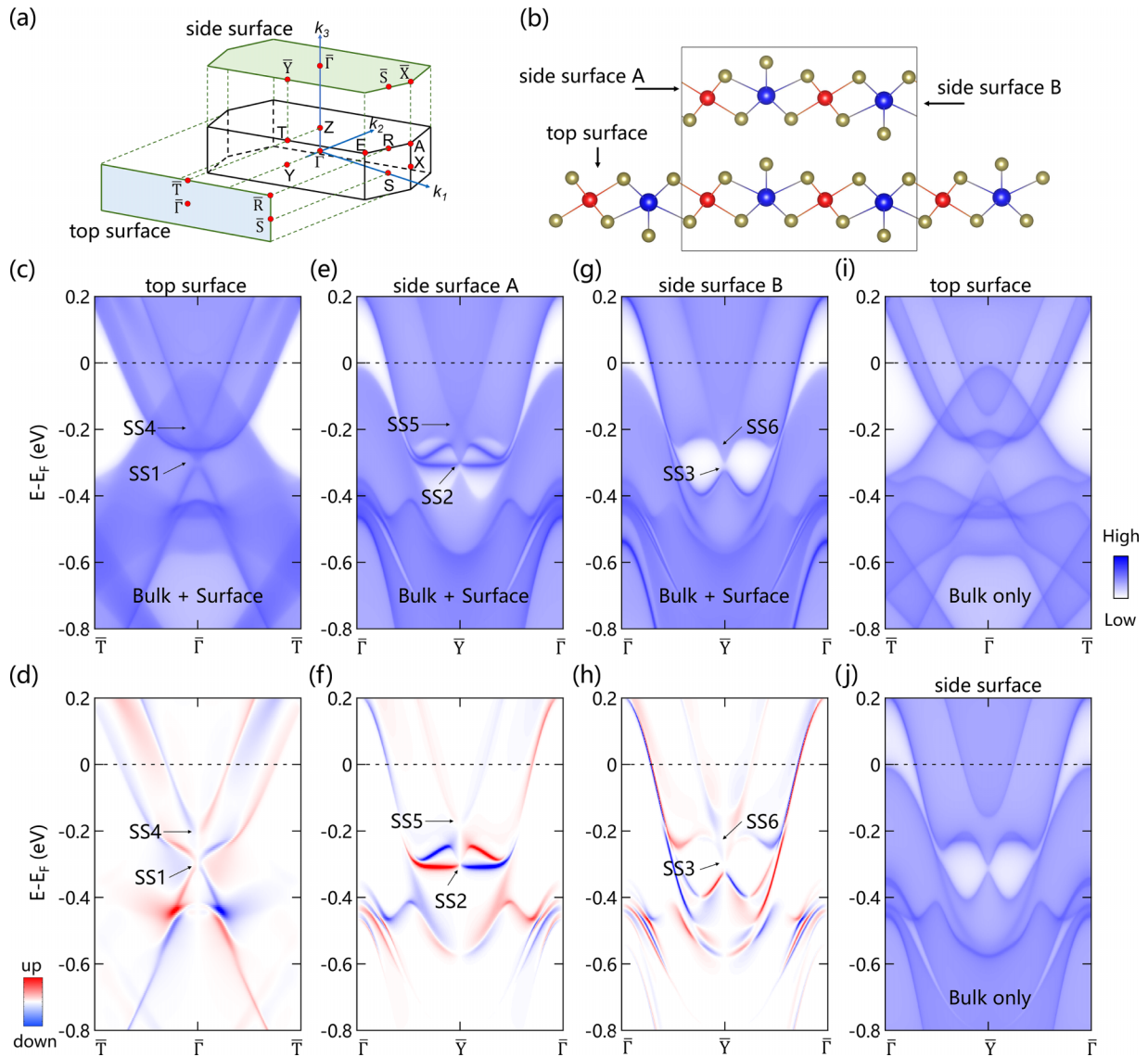


FIG. 6. Nontrivial surface states in NbNiTe₅. (a) Bulk Brillouin zone (black lines) and the projected surface Brillouin zones, with the light blue one for the surface perpendicular to b and the light green one for that perpendicular to c . (b) Crystal structure of NbNiTe₅ with three cleaved surfaces indicated by the black arrows. The top surface, parallel to NbNiTe₅ layers, is the most easily obtained surface. The side surfaces that we consider are perpendicular to the c axis, and they can be obtained by cleaving between Te-Te bonds, which both terminate with Te atoms but still have two types. (c) Calculated surface spectrum of both bulk and surface states along \bar{T} - $\bar{\Gamma}$ - \bar{T} on the top surface. (d) Spin-resolved surface spectrum corresponding to (c). (e),(f) Same as (c),(d) but along $\bar{\Gamma}$ - \bar{Y} - $\bar{\Gamma}$ on the side surface A. (g),(h) Same as (e),(f) but on the side surface B. (i) Calculated surface spectrum of only the bulk states along \bar{T} - $\bar{\Gamma}$ - \bar{T} on the top surface. (j) Same as (i) but on the side surface A or B.

NbNiTe₅. Our results clearly reveal its anisotropic transport properties due to its quasi-1D crystal structure. By the analysis of quantum dHvA oscillations, we identified three oscillation frequencies, all of which should originate from the Fermi surface composed of the nodal-line bands based on first-principles calculations, in common with its analogs TaTMTe₅. We associated the identified frequencies with the two small hole pockets H₁ and H₂ and the large hole pockets H₃ in qualitative comparison with the calculated bands. Our first-principles calculations demonstrate NbNiTe₅ is a candidate of multiple topological material. Besides the

nonsymmorphic symmetry-protected nodal lines and band inversion (anticrossing) induced topological surface states that have been reported in TaPtTe₅ [25] and TaNiTe₅ [27], a ladder of topological gaps with a coexistence of strong and weak topology and a series of induced topological surface states are identified. More experiments, such as ARPES and scanning tunneling microscopy/spectroscopy measurements, are highly desirable to probe the nontrivial surface and bulk states proposed in this study. Quasi-1D NbNiTe₅, highly feasible by mechanical exfoliation, provides another platform for investigations of low-dimensional topological physics.

ACKNOWLEDGMENTS

The authors would like to thank D. Qian, J. Wang, and X. G. Wan for fruitful discussions. This work was supported by Zhejiang Provincial Natural Science Foundation of China (Grant No. LZ23A040002) and the National Natural Science Foundation of China (Grants No. 12274369, No. 11974061,

No. U1932155, and No. 11504329). S.-Z.X. was supported by the National Natural Science Foundation of China (Grant No. 12204495). G.-H.C. acknowledges support from the Key Research and Development Program of Zhejiang Province, China (Grant No. 2021C01002).

W.-H.J. and S.-Z.X. contributed equally to this work.

-
- [1] N. P. Armitage, E. J. Mele, and A. Vishwanath, *Rev. Mod. Phys.* **90**, 015001 (2018).
- [2] B. Q. Lv, T. Qian, and H. Ding, *Rev. Mod. Phys.* **93**, 025002 (2021).
- [3] Z. J. Wang, Y. Sun, X. Q. Chen, C. Franchini, G. Xu, H. M. Weng, X. Dai, and Z. Fang, *Phys. Rev. B* **85**, 195320 (2012).
- [4] H. M. Weng, X. Dai, and Z. Fang, *J. Phys.: Condens. Matter* **28**, 303001 (2016).
- [5] Z. K. Liu, B. Zhou, Y. Zhang, Z. J. Wang, H. M. Weng, D. Prabhakaran, S. K. Mo, Z. X. Shen, Z. Fang, X. Dai, Z. Hussain, and Y. L. Chen, *Science* **343**, 864 (2014).
- [6] Z. K. Liu, J. Jiang, B. Zhou, Z. J. Wang, Y. Zhang, H. M. Weng, D. Prabhakaran, S. K. Mo, H. Peng, P. Dudin, T. Kim, M. Hoesch, Z. Fang, X. Dai, Z. X. Shen, D. L. Feng, Z. Hussain, and Y. L. Chen, *Nat. Mater.* **13**, 677 (2014).
- [7] Z. K. Liu, L. X. Yang, Y. Sun, T. Zhang, H. Peng, H. F. Yang, C. Chen, Y. Zhang, Y. F. Guo, D. Prabhakaran, M. Schmidt, Z. Hussain, S. K. Mo, C. Felser, B. Yan, and Y. L. Chen, *Nat. Mater.* **15**, 27 (2016).
- [8] S. Y. Xu, I. Belopolski, N. Alidoust, M. Neupane, G. Bian, C. L. Zhang, R. Sankar, G. Q. Chang, Z. J. Yuan, C. C. Lee, S. M. Huang, H. Zheng, J. Ma, D. S. Sanchez, B. K. Wang, A. Bansil, F. C. Chou, P. P. Shibayev, H. Lin, S. Jia *et al.*, *Science* **349**, 613 (2015).
- [9] X. G. Wan, A. M. Turner, A. Vishwanath, and S. Y. Savrasov, *Phys. Rev. B* **83**, 205101 (2011).
- [10] G. Bian, T. R. Chang, R. Sankar, S. Y. Xu, H. Zheng, T. Neupert, C. K. Chiu, S. M. Huang, G. Q. Chang, I. Belopolski, D. S. Sanchez, M. Neupane, N. Alidoust, C. Liu, B. K. Wang, C. C. Lee, H. T. Jeng, C. L. Zhang, Z. J. Yuan, S. Jia *et al.*, *Nat. Commun.* **7**, 10556 (2016).
- [11] J. Hu, Z. J. Tang, J. Y. Liu, X. Liu, Y. L. Zhu, D. Graf, K. Myhro, S. Tran, C. N. Lau, J. Wei, and Z. Q. Mao, *Phys. Rev. Lett.* **117**, 016602 (2016).
- [12] M. Neupane, S. Y. Xu, R. Sankar, N. Alidoust, G. Bian, C. Liu, I. Belopolski, T. R. Chang, H. T. Jeng, H. Lin, A. Bansil, F. C. Chou, and M. Z. Hasan, *Nat. Commun.* **5**, 3786 (2014).
- [13] T. Liang, Q. Gibson, M. N. Ali, M. Liu, R. J. Cava, and N. P. Ong, *Nat. Mater.* **14**, 280 (2015).
- [14] S. A. Parameswaran, T. Grover, D. A. Abanin, D. A. Pesin, and A. Vishwanath, *Phys. Rev. X* **4**, 031035 (2014).
- [15] X. C. Huang, L. X. Zhao, Y. J. Long, P. P. Wang, D. Chen, Z. H. Yang, H. Liang, M. Q. Xue, H. M. Weng, Z. Fang, X. Dai, and G. F. Chen, *Phys. Rev. X* **5**, 031023 (2015).
- [16] L. P. He, X. C. Hong, J. K. Dong, J. Pan, Z. Zhang, J. Zhang, and S. Y. Li, *Phys. Rev. Lett.* **113**, 246402 (2014).
- [17] Z. J. Xiang, D. Zhao, Z. Jin, C. Shang, L. K. Ma, G. J. Ye, B. Lei, T. Wu, Z. C. Xia, and X. H. Chen, *Phys. Rev. Lett.* **115**, 226401 (2015).
- [18] X. Xu, J. Jiang, W. J. Shi, V. Süß, C. Shekhar, S. C. Sun, Y. J. Chen, S.-K. Mo, C. Felser, B. H. Yan, H. F. Yang, Z. K. Liu, Y. Sun, L. X. Yang, and Y. L. Chen, *Phys. Rev. B* **99**, 195106 (2019).
- [19] Z. Hao, W. Chen, Y. Wang, J. Li, X. M. Ma, Y. J. Hao, R. Lu, Z. Shen, Z. Jiang, W. Liu, Q. Jiang, Y. Yang, X. Lei, L. Wang, Y. Fu, L. Zhou, L. Huang, Z. Liu, M. Ye, D. Shen *et al.*, *Phys. Rev. B* **104**, 115158 (2021).
- [20] S. M. Young and C. L. Kane, *Phys. Rev. Lett.* **115**, 126803 (2015).
- [21] C. Fang, H. Weng, X. Dai, and Z. Fang, *Chin. Phys. B* **25**, 117106 (2016).
- [22] W. H. Jiao, X. M. Xie, Y. Liu, X. Xu, B. Li, C. Q. Xu, J. Y. Liu, W. Zhou, Y. K. Li, H. Y. Yang, S. Jiang, Y. K. Luo, Z. W. Zhu, and G. H. Cao, *Phys. Rev. B* **102**, 075141 (2020).
- [23] C. Q. Xu, Y. Liu, P. G. Cai, B. Li, W. H. Jiao, Y. L. Li, J. Y. Zhang, W. Zhou, B. Qian, X. F. Jiang, Z. X. Shi, R. Sankar, J. L. Zhang, F. Yang, Z. W. Zhu, P. Biswas, D. Qian, X. L. Ke, and X. F. Xu, *J. Phys. Chem. Lett.* **11**, 7782 (2020).
- [24] W. H. Jiao, S. Xiao, B. Li, C. Xu, X.-M. Xie, H. Q. Qiu, X. Xu, Y. Liu, S. J. Song, W. Zhou, H. F. Zhai, X. Ke, S. He, and G. H. Cao, *Phys. Rev. B* **103**, 125150 (2021).
- [25] S. Xiao, W. H. Jiao, Y. Lin, Q. Jiang, X. Yang, Y. He, Z. Jiang, Y. Yang, Z. Liu, M. Ye, D. Shen, and S. He, *Phys. Rev. B* **105**, 195145 (2022).
- [26] Y. L. Li, Z. Ran, C. Z. Huang, G. Y. Wang, P. Y. Shen, H. L. Huang, C. Q. Xu, Y. Liu, W. H. Jiao, W. X. Jiang, J. Y. Hu, G. C. Zhu, C. H. Xu, Q. Lu, G. H. Wang, Q. Jing, S. Y. Wang, Z. W. Shi, J. F. Jia, X. F. Xu *et al.*, *Phys. Rev. Lett.* **128**, 106802 (2022).
- [27] D. Y. Wang, Q. Jiang, K. Kuroda, K. Kawaguchi, A. Harasawa, K. Yaji, A. Ernst, H. J. Qian, W.-J. Liu, H.-M. Zha, Z.-C. Jiang, N. Ma, H.-P. Mei, A. Li, T. Kondo, S. Qiao, and M. Ye, *Phys. Rev. Lett.* **129**, 146401 (2022).
- [28] E. W. Liimatta and J. A. Ibers, *J. Solid State Chem.* **71**, 384 (1987).
- [29] W. H. Jiao, S. Xiao, S. J. Zhang, W. Z. Yang, X. M. Xie, Y. Liu, J. Y. Liu, S. J. Song, W. Liu, Z. Ren, G. H. Cao, X. Xu, and S. He, *Phys. Rev. B* **105**, 064201 (2022).
- [30] See Supplemental Material at <http://link.aps.org/supplemental/10.1103/PhysRevB.107.195124> for detailed EDS results, Hall data and the bulk \mathbb{Z}_2 topological indices based on the Wilson loop calculations.
- [31] K. Momma and F. Izumi, *J. Appl. Crystallogr.* **41**, 653 (2008).
- [32] P. Giannozzi, S. Baroni, N. Bonini, M. Calandra, R. Car, C. Cavazzoni, D. Ceresoli, G. L. Chiarotti, M. Cococcioni, I. Dabo, A. D. Corso, S. Gironcoli, S. Fabris, G. Fratesi, R. Gebauer, U. Gerstmann, C. Gougoussis, A. Kokalj, M. Lazzeri, L. Martin-Samos *et al.*, *J. Phys.: Condens. Matter* **21**, 395502 (2009).

- [33] J. P. Perdew, K. Burke, and M. Ernzerhof, *Phys. Rev. Lett.* **77**, 3865 (1996).
- [34] P. M. C. Rourke and S. R. Julian, *Comput. Phys. Commun.* **183**, 324 (2012).
- [35] G. Pizzi, V. Vitale, R. Arita, S. Blugel, F. Freimuth, G. Geranton, M. Gibertini, D. Gresch, C. Johnson, T. Koretsune, J. Ibanez-Azpiroz, H. Lee, J. Lihm, D. Marchand, A. Marrazzo, Y. Mokrousov, J. I. Mustafa, Y. Nohara, Y. Nomura, L. Paulatto *et al.*, *J. Phys.: Condens. Matter* **32**, 165902 (2020).
- [36] Q. Wu, S. Zhang, H.-F. Song, M. Troyer, and A. A. Soluyanov, *Comput. Phys. Commun.* **224**, 405 (2018).
- [37] D. Cvijović, *Theor. Math. Phys.* **166**, 37 (2011).
- [38] M. N. Ali, J. Xiong, S. Flynn, J. Tao, Q. D. Gibson, L. M. Schoop, T. Liang, N. Haldolaarachchige, M. Hirschberger, N. P. Ong, and R. J. Cava, *Nature (London)* **514**, 205 (2014).
- [39] Y. Li, L. Li, J. Wang, T. Wang, X. Xu, C. Xi, C. Cao, and J. Dai, *Phys. Rev. B* **94**, 121115(R) (2016).
- [40] D. J. Kim, J. Xia, and Z. Fisk, *Nat. Mater.* **13**, 466 (2014).
- [41] S. Wolgast, Ç. Kurdak, K. Sun, J. W. Allen, D. J. Kim, and Z. Fisk, *Phys. Rev. B* **88**, 180405(R) (2013).
- [42] Y. L. Wang, L. R. Thoutam, Z. L. Xiao, J. Hu, S. Das, Z. Q. Mao, J. Wei, R. Divan, A. Luican-Mayer, G. W. Crabtree, and W. K. Kwok, *Phys. Rev. B* **92**, 180402(R) (2015).
- [43] D. Shoenberg, *Magnetic Oscillations in Metals* (Cambridge University Press, Cambridge, England, 1984).
- [44] G. P. Mikitik and Y. V. Sharlai, *Phys. Rev. Lett.* **82**, 2147 (1999).
- [45] J. Hu, Z. J. Tang, J. Y. Liu, Y. L. Zhu, J. Wei, and Z. Q. Mao, *Phys. Rev. B* **96**, 045127 (2017).
- [46] A. Alexandradinata, C. Wang, W. Duan, and L. Glazman, *Phys. Rev. X* **8**, 011027 (2018).
- [47] X. A. Nie, S. Li, M. Yang, Z. Zhu, H.-K. Xu, X. Yang, F. Zheng, D. Guan, S. Wang, Y.-Y. Li, C. Liu, J. Li, P. Zhang, Y. Shi, H. Zheng, and J. Jia, *ACS Nano* **14**, 2366 (2020).